Numerical simulation for the prediction of the plate motions:
Effects of lateral viscosity variations in the lithosphere

Masaki Yoshida[1], Satoru Honda[2], Motoyuki Kido[3], and Yasuyuki Iwase[4]

[1]*Division of Geodynamics, Earthquake Research Institute, University of Tokyo, 1-1-1 Yayoi, Bunkyo-ku, Tokyo 113-0032, Japan*
[2]*Department of Earth and Planetary Systems Science, Graduate School of Science, Hiroshima University,*
1-3-1 Kagamiyama, Higashi-hiroshima, Hiroshima 739-8526, Japan
[3]*Frontier Research Program for Subduction Dynamics, Japan Marine Science and Technology Center,*
2-15 Natsushima-cho, Yokosuka, Kanagawa 237-0061, Japan
[4]*Department of Earth and Ocean Sciences, School of Applied Sciences, National Defense Academy,*
1-10-20 Hashirimizu, Yokosuka, Kanagawa 239-8686, Japan

A numerical simulation of Newtonian viscous flow without inertia terms in a 3-D spherical shell driven by the negative buoyancy due to the slabs has been conducted to understand the effects of weak plate margins on the plate motions. Density loads are inferred from the seismicity and the reconstruction of the subduction history. The toroidal energy of plate motion comparable to the poloidal energy appears, when γ (ratio of the viscosity at margins to that of interiors) becomes $O(0.01)$. For the whole mantle density model, all the plates move too fast relative to the Pacific plate. The direction of major plate motions is generally improved by the inclusion of weak plate boundaries. The density loads in the upper mantle appear to explain the overall plate motions, although some of the plate motions may require hidden and/or deeper density anomalies to be consistent with the observations. As γ decreases, the geoid anomalies associated with the upper mantle slabs change their signs. This reversal affects the long-wavelength components of the geoid anomalies. A considerable part of the horizontal stress field shows a horizontal extension suggesting that another type of density anomalies is necessary to explain the general compressional field of the real Earth.

1. Introduction

In the past about 20 years, using a realistic density distribution inferred from the subducted slabs and the seismic tomography, many workers treated the mantle as a fluid with depth-dependent viscosity, and they obtained a reasonable configuration of geoid anomalies (e.g., Hager, 1984; Hager *et al.*, 1985) and the motion of the plates (e.g., Ricard and Vigny, 1989). On the other hand, from the laboratory measurements, the viscosity of the Earth's mantle is believed to be a strong function of pressure, stress, composition and temperature (e.g., Karato and Wu, 1993). Thus, we expect considerable lateral variations in viscosity.

Analytical solutions using the traditional propagator matrix method (e.g., Hager and O'Connel, 1981; Hager and Clayton, 1989) or the green functions (Corrieu *et al.*, 1995) are restricted to the spherically symmetric viscosity structure, because of the mathematical difficulties arising from the "mode coupling" caused by the lateral viscosity variations (Richards and Hager, 1989). When we treat the complicated arbitrary lateral viscosity variations in the mantle, numerical approaches are more appropriate. With a numerical model of flow within a 3-D spherical shell, some studies focused on the effects which a long-wavelength lateral

viscosity variation has on geoid anomalies, topography or plate velocities (Richards and Hager, 1989; Zhang and Christensen, 1993). They concluded that the longest wavelength geoid anomalies are not seriously affected by the lateral viscosity variations. Using the modal approaches, Wen and Anderson (1997) included the viscosity difference between the continental and the oceanic plates in the model in which the driving forces are the density anomalies inferred from the seismic tomography and the slab distribution. They showed that such a viscosity difference can explain the observed large-scale poloidal and toroidal plate motions.

The mantle flow produces shear stresses at the base of the lithosphere. Intraplate stress field is related to the forces acting on the lithosphere and, some have argued that it contains information on the driving mechanism of plates (Richardson, 1992). Most intraplate or midplate regimes are characterized by a compressional stress, and the extensional stress regimes are localized to the elevated areas. There is a strong positive correlation between the maximum horizontal directions in broad regions of plates and the absolute plate motions (Zoback *et al.*, 1989; Zoback, 1992). This implies that the shear stress distribution at the base of the lithosphere is closely related to the plate motion. So far, little attention has been devoted to the intraplate stress problem using a 3-D model of a viscous Earth. For example, Bai *et al.* (1992) computed the surface stress field obtained by the density

heterogeneity derived from the seismic tomography and the slab distribution, assuming no interaction of the plates.

Because of the stress dependence of viscosity and faulting, the largest lateral variations of the effective viscosity may occur near the plate boundaries (Zhong and Gurnis, 1996). These lateral viscosity variations may influence plate motions and the geoid anomalies. For example, Moresi and Gurnis (1996) suggested that the regional modeling of the geoid anomalies is very sensitive to the lateral strength variation of the subducted slab. Recently, Zhong and Davies (1999) found, by the finite element modeling, that the plate rheology such as stiff plate interiors and weak plate margins affect the long-wavelength geoid anomalies significantly, and they were able to reproduce the basic features of the observed geoid anomalies and the present-day plate motions. They also studied the effects of rheology of subducted slabs and showed that the weak slabs can explain the geoid anomalies better than the stiff slabs can. However, they did not analyze in detail the surface velocity field, stress distribution within plates, nor the influence weak plate margins on the results. In this paper, we study, using a numerical technique, instantaneous viscous flow within a 3-D spherical shell driven by internal buoyancy forces. The buoyancy forces arise from subducted slabs. And we specifically focus on the influence which lateral variations in lithospheric viscosity on the present-day plate motions, the geoid anomalies and intraplate stresses. We also study the effects of the different density models on the observables.

2. Methods
2.1 Basic equations

The flow of an incompressible Newtonian fluid without inertia terms is governed by the following equations describing the conservation of mass and momentum,

$$\nabla \cdot \boldsymbol{v} = 0, \tag{1}$$

$$0 = \nabla \cdot \boldsymbol{\sigma} + \delta\rho g \, \boldsymbol{e}_r, \tag{2}$$

where $\boldsymbol{v}$ is the velocity vector, $\boldsymbol{\sigma}$ is the total stress tensor, $\delta\rho$ is the density anomaly, g is the gravitational acceleration and $\boldsymbol{e}_r$ is the unit vector for the radial direction (positive upward).

The total stress tensor $\boldsymbol{\sigma}$ may be separated into the isotropic and deviatoric components,

$$\boldsymbol{\sigma} = -p \, \boldsymbol{I} + \boldsymbol{\tau}, \tag{3}$$

where p is the pressure, $\boldsymbol{I}$ is the identity matrix and $\boldsymbol{\tau}$ is the deviatoric stress tensor.

The deviatoric stress tensor $\boldsymbol{\tau}$ may be given by,

$$\boldsymbol{\tau} = 2\eta \, \dot{\boldsymbol{\varepsilon}}, \tag{4}$$

where η is the dynamic viscosity and $\dot{\boldsymbol{\varepsilon}}$ is the strain rate tensor given by,

$$\dot{\boldsymbol{\varepsilon}} = \frac{1}{2} \left\{ \nabla \boldsymbol{v} + [\nabla \boldsymbol{v}]^T \right\}, \tag{5}$$

where $[\ ]^T$ indicates a tensor transpose.

The boundary conditions at the Earth's surface and the core-mantle boundary are impermeable and free-slip, that is,

$$\boldsymbol{v} \cdot \boldsymbol{e}_r = 0 \quad (\text{at } r = r_0, r_1), \tag{6a}$$

$$\sigma_{r\theta} = \sigma_{r\phi} = 0 \quad (\text{at } r = r_0, r_1), \tag{6b}$$

where r_0 and r_1 are the radius of the Earth's core and the Earth, respectively. The dynamic topographies of the bottom (i.e., CMB) and top surfaces may be given by,

$$\delta h_{0l}^m = -\frac{\sigma_{rr}(r_0)_l^m}{\Delta\rho_0 g}, \tag{7a}$$

$$\delta h_{1l}^m = \frac{\sigma_{rr}(r_1)_l^m}{\Delta\rho_1 g}, \tag{7b}$$

where $\sigma_{rr}(r_0)_l^m$ and $\sigma_{rr}(r_1)_l^m$ are the spherical harmonic expansions (degree l and order m) of the normal stress at the CMB and top surfaces, respectively. $\Delta\rho_0$ and $\Delta\rho_1$ are the density contrast at the CMB and the top surfaces, respectively. The spherical harmonic expansion of the geoid anomalies ($\delta N_l^m (r_1)$) anomalies caused by the internal density anomalies ρ_l^m and the dynamic topographies, may be given by,

$$\delta N_l^m(r_1) = \frac{4\pi G}{g(2l+1)} \left[\int_{r_0}^{r_1} \rho_l^m(r) r \left(\frac{r_0}{r_1}\right)^{l+1} dr \right.$$
$$+ \frac{\sigma_{rr}(r_1)_l^m}{g} r_1$$
$$\left. - \frac{\sigma_{rr}(r_0)_l^m}{g} r_0 \left(\frac{r_0}{r_1}\right)^{l+1} \right], \tag{8}$$

where G is the universal gravitational constant, $\rho_l^m(r)$ is the spherical harmonic expansion of the internal density anomaly (e.g., Hager, 1984; Hager *et al.*, 1985; Hager and Clayton, 1989).

The coefficients of the spherical harmonic expansion of poloidal and toroidal velocities are obtained by an integration over the sphere. For poloidal coefficients,

$$a_{slm} = \frac{1}{4\pi l(l+1)} \int_S \left(v_\theta \frac{\partial Y_l^m}{\partial \theta} + \frac{v_\phi}{\sin\theta} \frac{\partial Y_l^m}{\partial \phi} \right) dS, \tag{9a}$$

and for toroidal coefficients,

$$a_{tlm} = \frac{1}{4\pi l(l+1)} \int_S \left(\frac{v_\theta}{\sin\theta} \frac{\partial Y_l^m}{\partial \phi} - v_\phi \frac{\partial Y_l^m}{\partial \theta} \right) dS, \tag{9b}$$

where Y_l^m is a spherical harmonic function (Hager and O'Connell, 1978). The poloidal and toroidal energies can be calculated by,

$$\sigma_{sl}^2 = \sum_{m=0}^{l} a_{slm}^2, \tag{10a}$$

$$\sigma_{tl}^2 = \sum_{m=0}^{l} a_{tlm}^2, \tag{10b}$$

Table 1. Physical parameters.

Symbol	Notation	Dimensional value
r	radial distances	
θ	latitude	
ϕ	longitude	
e_r, e_θ, e_ϕ	unit vector for r, θ and ϕ directions	
v	velocity vector	
σ	stress tensor	
ρ	density	
$\delta\rho$	density anomaly	see text
p	dynamic pressure	
τ	deviatoric stress tensor	
I	identity matrix	
$\dot{\varepsilon}$	strain rate tensor	
η	dynamic viscosity	see text
r_1	radius of the Earth	6.371×10^6 [m]
r_0	radius of the Earth's core	3.471×10^6 [m]
G	universal gravitational constant	6.67×10^{-11}
$\Delta\rho_1$	density contrast at the surface	3.4×10^3 [kg/m^3]
$\Delta\rho_0$	density contrast at the CMB	4.3×10^3 [kg/m^3]
g	gravity acceleration	10 [m/sec^2]
α	thermal expansivity	2.0×10^{-5} [1/K]
d	thickness of the mantle ($r_1 - r_0$)	2.9×10^6 [m]
κ	thermal diffusivity	1.0×10^{-6} [m^2/sec]
δh_1	dynamic topography at the surface	
δh_0	dynamic topography at the CMB	
δN	geoid anomaly	

respectively. The meanings of the symbols and the physical parameters used in this study are summarized in Table 1.

Basic equations (Eqs. (1) and (2)) are discretized by the control volume method (Iwase, 1996). Radial, latitudinal and longitudinal resolutions are 43, 100 and 200 units, respectively. They are equally divided into each direction. A test of resolution was conducted by comparing the results with those of half-analytic methods (e.g., Hager, 1984) for the cases with no lateral change of viscosity. The results are summarized in Table 3 for constant and reference viscosity (radially stratified viscosity structure: See 2.2.2) models using the density model of W (See 2.2.1). They are the root mean square (RMS) misfits of degree l components of geoid anomalies, top and CMB surface topographies and poloidal velocity field. The case with a constant viscosity gives satisfactory results (total RMS misfit of $\approx 1\%$), while the cases with radial variations of viscosity do not show a good fit (total RMS misfit of $2 \sim 7\%$). Although we have a possibility that these misfits may arise from a poor resolution and/or numerical error, we believe that the non-negligible fraction of misfit comes from the difficulty of treatment of a viscosity jump at a depth using the control volume approach. We found that the toroidal field is almost absent and the difference of the velocity field mainly comes from that of the

Table 2. Density models. Subduction history model is expressed by a spherical harmonic expansion degree up to 15 (Ricard *et al.*, 1993).

Model	Upper mantle	Lower mantle
U1	seismic slab	no loads
U2	subduction history	no loads
W	subduction history	subduction history

magnitude and not from the direction of the velocity. This may suggest the existence of effective depth of the viscosity jump. Actually, the fit of geoid anomalies becomes slightly better ($\approx 6\%$), if we vary the depth of viscosity jump, which is within a resolution of a control volume, for the calculation of half-analytic solutions. However the misfit of velocity becomes worse ($\approx 4\%$) for this case. Thus, the misfit of a several percents may easily comes from the ambiguity of the equivalent analytic model. Since the misfits of geoid anomalies become significantly large when l is larger than 9, we only show the spherical harmonic components less than $l = 10$ for the discussion of geoid anomalies.

Table 3. The RMS misfits of degree *l* components of geoid anomalies, surface and CMB topographies and the poloidal velocity in unit of %. Constant viscosity (Top) and reference viscosity (Bottom) models.

l	2	3	4	5	6	7	8	9	10	11	12	13	14	15	Total
Geoid	0.9	1.0	1.2	1.3	1.6	1.9	2.1	2.3	2.7	3.5	3.1	3.9	4.2	4.7	1.3
Surface	0.4	0.6	0.7	0.8	1.0	1.1	1.3	1.4	1.7	2.3	1.8	2.5	2.5	2.8	1.0
CMB	0.6	0.9	1.1	1.1	1.2	1.2	1.3	1.3	1.3	1.3	1.4	1.4	1.5	1.3	1.1
Velocity	0.0	0.1	0.0	0.1	0.1	0.3	0.4	0.5	0.8	1.4	1.3	1.7	2.1	2.3	0.1

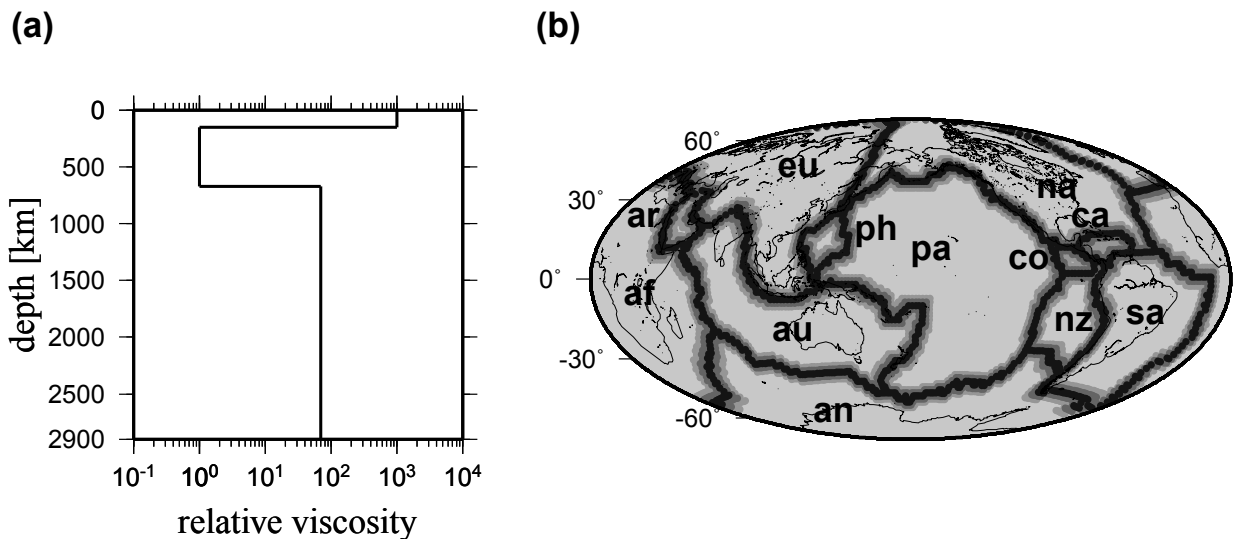| *l*	2	3	4	5	6	7	8	9	10	11	12	13	14	15	Total
Geoid	8.0	6.0	7.6	7.5	9.1	8.1	5.8	6.9	12.6	12.6	25.2	27.1	42.6	42.6	7.3
Surface	2.4	2.9	3.2	3.3	3.5	2.5	1.6	1.2	2.4	3.9	5.1	7.2	7.6	8.9	3.0
CMB	0.7	1.2	1.5	1.4	1.4	1.2	1.3	1.3	1.3	1.3	1.4	1.4	1.5	1.3	1.0
Velocity	1.0	1.8	2.8	3.9	5.2	5.6	6.3	6.9	6.9	4.0	4.4	2.8	2.6	4.8	1.3

(a)   **(b)**

Fig. 1. (a) Radial viscosity profile of the reference model. 3-layered model is adopted: the lithosphere (0 km to 150 km), the upper mantle (150 km to 670 km) and the lower mantle (670 km to 2900 km). (b) Horizontal variations of viscosity in the lithosphere (0 km to 150 km). Lithosphere is divided into 12 main plates (light parts) and the weak plate margins (dark parts). The abbreviation 'af' means the African plate, 'an' the Antarctic, 'ar' the Arabian, 'au' the Australian, 'ca' the Caribbean, 'co' the Cocos, 'eu' the Eurasian, 'na' the Nazca, 'na' the North American, 'pa' the Pacific, 'ph' the Philippine Sea, and 'sa' the South American. Continental shore lines are also shown.

2.2 Models

2.2.1 Density models

Following Zhong and Davies (1999), a reference internal density load, which drives the plates, is assumed to be only negative buoyancy due to the subducted slabs. The positive buoyancy due to the hot upwelling (plume) is neglected in our models. Since the Earth's mantle is considerably heated from within by the radioactive elements, the cold subducted slabs would be the main source of the driving force and dominate the heterogeneity structure in the mantle. Moreover, Tackley (1998) suggested that the large low seismic velocity regions in the lower mantle may be neutrally buoyant because of the balance between the positive thermal buoyancy and the negative chemical buoyancy. Based on the uplift of Africa as well as its uplift rate, however, Gurnis *et al.* (2000) argued that lower mantle is positive buoyancy (low velocity).

In this study, we use three mantle density heterogeneity models (U1, U2 and W) as summarized in Table 2 and described below. First, we use the model inferred from the study of the history of the subduction for the past 180 Myr (Ricard *et al.*, 1993) inferred from the Cenozoic and Mesozoic plate reconstruction (Gordon and Jurdy, 1986). The density anomalies of their original model are expanded by spherical harmonics up to degree 15 for whole mantle. We call this whole mantle model, 'W model'. Second, to see the contribution from the upper mantle density anomalies, we omit the lower mantle density heterogeneity of W model. We call this upper mantle model 2, 'U2 model', hereafter. Third, we assume that the density heterogeneities of the upper mantle exist only where the seismicity is observed (e.g., Hager, 1984). Seismic hypocentres (the magnitude is greater than 5) reported from 1964 to 1987 in the International Seis-

mological Centre (ISC) bulletin, are scanned and mapped into the control volumes of the numerical models. We omit the earthquakes whose hypocentral depth is less than 100 km to remove the intraplate earthquakes. Following Hager and Clayton (1989) the mass anomaly of the lithosphere before the subduction is assumed to be 8×10^5 g/cm^2 for the plate thickness of 125 km, regardless of the slab ages. This corresponds to an average density anomaly of 64 kg/m^3 at all depths (Hager, 1984). We call this upper mantle model 1, 'U1 model'.

2.2.2 Viscosity models As a reference viscosity model, the 3-layered viscosity model is adopted, that is, the lithosphere (0 km to 150 km), the upper mantle (150 km to 670 km) and the lower mantle (670 km to 2900 km). In reality, the viscosity varies through a several finite volumes so that the viscosity change within a finite volume is 10 or less. Using the W model and the geoid anomalies, Corrieu *et al.* (1995) concluded that the relative viscosity variation of 30 (lithosphere), 1 (upper mantle) and 70 (lower mantle) without the lateral variation is the best model to explain the geoid anomalies. In our simulation, in order to focus on the influence of stiff 'high viscous' plate interiors and weak 'low viscous' plate margins, the viscosity of plate interiors is taken to be 1000 times that of the upper mantle, keeping the relative viscosity of the lower mantle 70 times greater than that of the upper mantle (Fig. 1(a)).

The plate margin is represented by a series of control volumes in the lithosphere, through which the plate boundaries run. The width of plate margin is set to 5 control volumes, and we set that the viscosity change in a control volume is less than 30. Note that, since the size of control volume changes along the latitude, this choice of plate margin yields the non-uniform weak plate boundary. The plate boundaries define 12 plates (Fig. 1(b)): the African (af), the Antarctic (an), the Arabian (ar), the Australian (au), the Caribbean (ca), the Cocos (co), the Eurasian (eu), the Nazca (nz), the North American (na), the Pacific (pa), the Philippine Sea (ph) and the South American (sa) plates. We define the ratio of the viscosity at plate margins to that of the plate interior,

$$\gamma \equiv \frac{\eta_{\text{marg}}}{\eta_{\text{pint}}}, \tag{11}$$

where η_{marg} and η_{pint} are the viscosities of plate margins and the plate interior, respectively. In this study, γ is taken to be either 1 (i.e., no plate margin), 0.1, 0.01, or 0.001 (the same viscosity as that of the upper mantle). The absolute viscosity of the upper mantle is set to 3.0×10^{20} Pa·s when we scale the results.

3. Results
3.1 Plate motion

The observed plate motions in a no-net-rotation (NNR) reference frame (Argus and Gordon, 1991) are shown in Fig. 2. Here, we use this to evaluate the surface motions obtained from our numerical results. Figures 3(a), (b) and (c) show the surface motions, derived from U1, U2 and W for various values of γ. These surface motions are obtained by subtracting the net rotation, which is equivalent to the degree 1 of toroidal components, from the calculated velocity field. However, we found that the component of the net
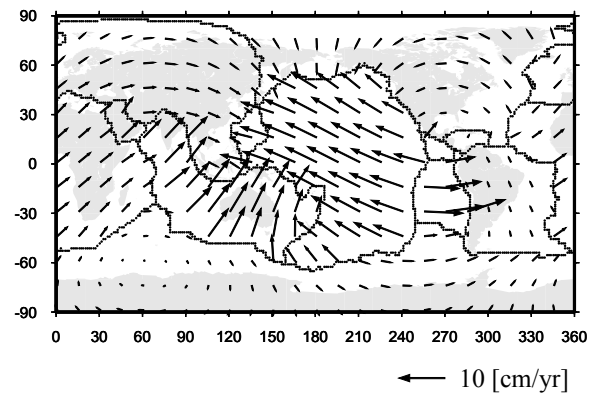

Fig. 2. Observed plate motion relative to the no-net-rotation (NNR) reference frame (Argus and Gordon, 1991).

rotation is negligibly small.

A general pattern of the plate motion such as the northeast movement of the Australian plate can be obtained even for the case with $\gamma = 1$ (i.e., no lateral viscosity variation). Inclusion of the weak plate margins makes the movement more plate-like and faster (e.g., Zhong and Davies, 1999). Looking at the Pacific plate at $\gamma = 0.001$ (Fig. 3), we see an abrupt change of velocity along the plate boundaries, which is a characteristics of the plate tectonic movement. However, we also see a possible internal deformation in some area such as Western Pacific. This may be caused by the non-uniform representation of weak plate margins.

Hager and O'Connell (1978) found that the toroidal energy is almost as large as the poloidal energy by the analysis of observed plate velocities. For $\gamma = 1$, that is, the viscosity without horizontal variation, the toroidal energy of the thermal convection is theoretically zero (Christensen and Harder, 1991). Thus, Hager and O'Connell's finding was considered as a characteristics of plate motion. Figure 4 shows the calculated poloidal and toroidal energies for given γ. With the decrease of the viscosity at plate margin, the toroidal components are excited. When $\gamma < 0.01$, the toroidal and poloidal energies become comparable.

To quantify the results more clearly, we introduce the ratio of RMS velocity of each 12 plates obtained from the calculation to that of the observations,

$$r_{\text{c/o}}(p) \equiv \sqrt{\frac{\frac{1}{S_{\text{p}}} \int v_{\text{cal}}^2 dS_{\text{p}}}{\frac{1}{S_{\text{p}}} \int v_{\text{obs}}^2 dS_{\text{p}}}}, \tag{12}$$

where v_{cal} is the surface velocity obtained from the calculation, v_{obs} is the observed velocity (i.e., NNR). S_{p} is the surface area of plate "p". Since the absolute value of the calculated velocity (or $r_{\text{c/o}}(p)$) is scaled by the absolute value of viscosity, which is a free parameter, it is preferable to normalize $r_{\text{c/o}}(p)$ by that of the reference plate such as the Pacific plate. Thus, we introduce

$$v_{\text{c/o}} \equiv \frac{r_{\text{c/o}}(p)}{r_{\text{c/o}}(pa)}, \tag{13}$$

where "pa" implies the Pacific plate.

(a)

$\gamma = 1$

$\gamma = 0.1$

$\gamma = 0.01$

$\gamma = 0.001$

(b)

$\gamma = 1$

$\gamma = 0.1$
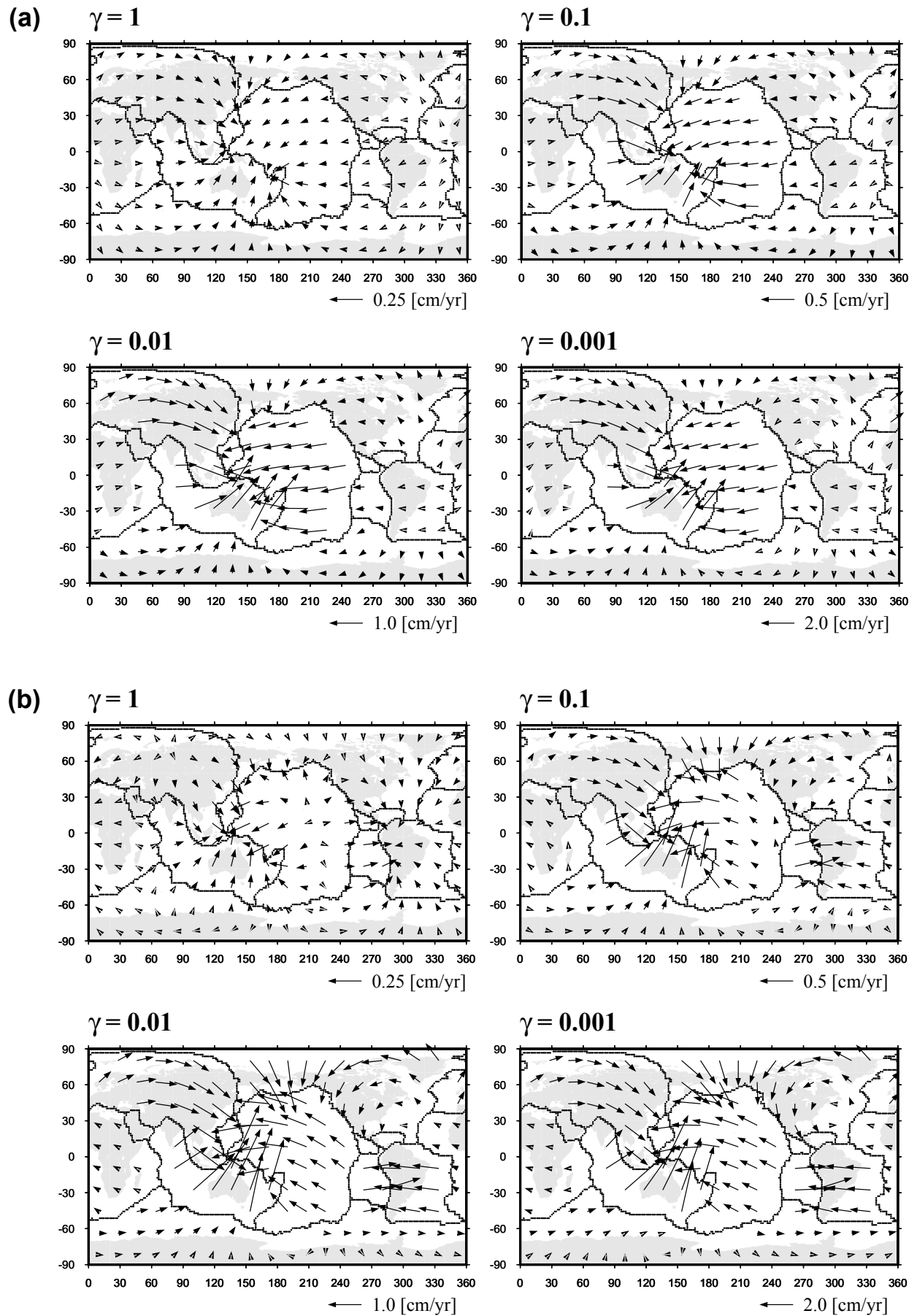
$\gamma = 0.01$

$\gamma = 0.001$

Fig. 3. (a) Calculated surface plate motion for the U1 model with various γ. (b) The same figure as Fig. 3(a) for the U2 model. (c) The same figure as Fig. 3(a) for the W model. In all the maps, plate boundaries and continents are shown.
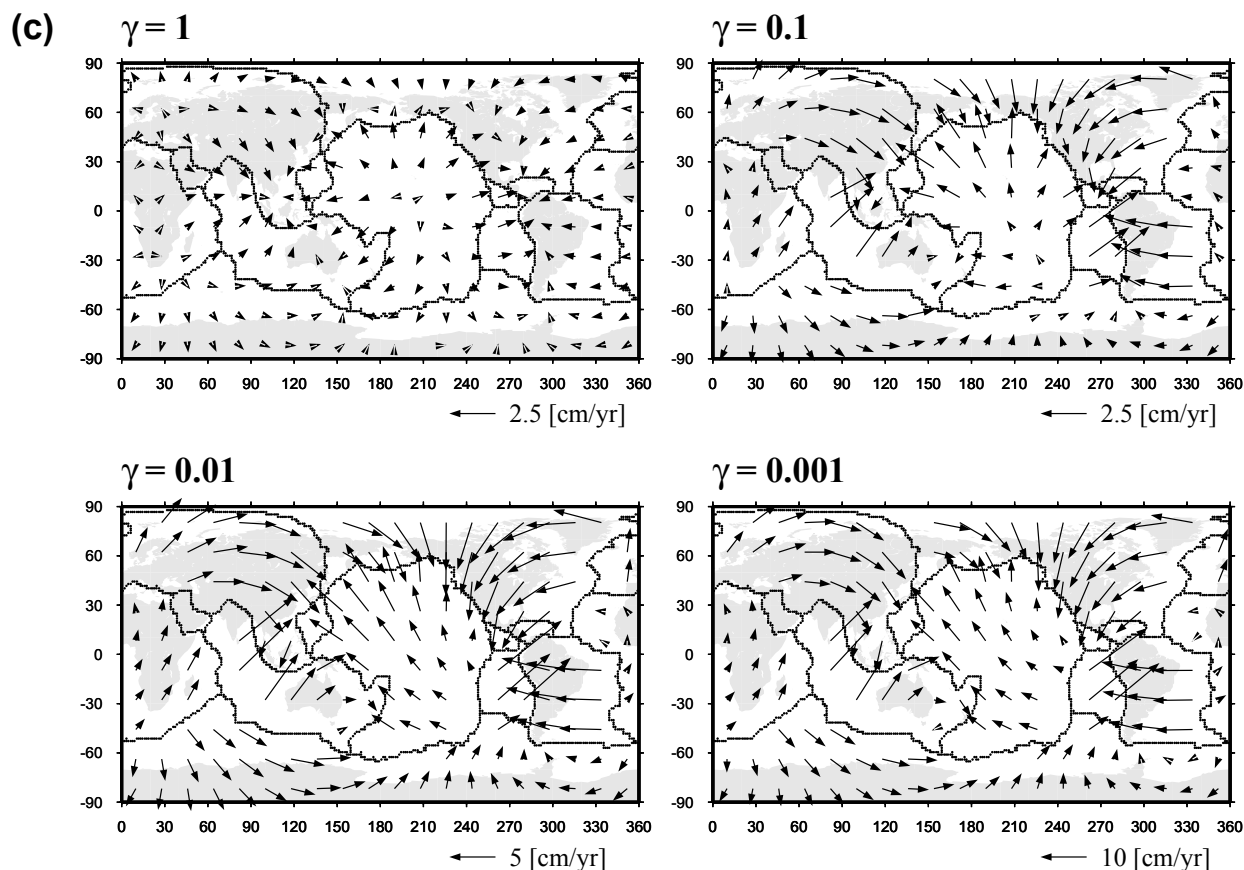
Fig. 3. (continued).

We also define the RMS difference of the azimuth of the velocity between the calculation and the observation, that is,

$$\Delta\Theta \equiv \sqrt{\frac{1}{S_p} \int (\Theta_{\text{cal}} - \Theta_{\text{obs}})^2 dS_p}, \qquad (14)$$

where Θ_{cal} is the azimuth of the surface motions obtained from the calculation and Θ_{obs} is the observed azimuth of the plate motions. Complete matching between the model calculations and the observations imply $v_{c/o} = 1$ and $\Delta\Theta = 0$.

Figures 5(a) and (b) show the $v_{c/o}$ and $\Delta\Theta$ of 12 plates as a function of γ for all the density models. In Fig. 5, "gl" implies the global average of $v_{c/o}$ and $\Delta\Theta$. However, for $v_{c/o}$, we exclude the Pacific plate, since its value is always one. They are shown in order of the plate size.

Tables 4 and 5 are the summaries of the results. In these tables, "+" and "−" show the improvement or degradation of the models by a decrease of γ. If the change of values is less than 20%, we show them in the brackets. In the last column, the names of the model which gives the best improvements are given. We show all the model names whose $v_{c/o}$ or $\Delta\Theta$ is within 20% of the best model. Other model names are also shown in the brackets in the order of degree of improvements.

$v_{c/o}$ for W model shows a systematic deviation, that is, all the plates move too fast relative to the Pacific plate (i.e., $v_{c/o} > 1$) (Fig. 5(a) and Table 4). Compared to whole mantle density model (W), $v_{c/o}$ of the upper mantle density models

(U1 and U2), is scattered around one and its global average is closer to one than that of W model is. Globally, the direction of plate motions is improved with a decrease of γ (Fig. 5(b) and Table 5). This improvement mainly comes from that of the major plates such as the Pacific, the Africa and the European plates. By looking at individual plates, we see that the direction of motion of the Nazca plate is greatly improved, if we use U2 or W model. Since both U2 and W models contain the aseismic part of the subducting slabs, this may imply a significant contribution of aseismic slabs and/or lower mantle density anomalies to the driving force of the Nazca plate.

3.2 Geoid

Figure 6 shows the observed geoid anomalies for $2 \le l \le 15$ (a) and $4 \le l \le 9$ (b). The geoid anomalies for $4 \le l \le 9$ is thought to be closely related to the existence of slabs (Hager, 1984). The obtained geoid anomalies for all the density models are shown in Fig. 7. The results are shown by the spherical harmonic expansion up to degree 9. Our calculated geoid anomalies for U1 and U2 at $\gamma = 1$ shows the opposite sign to the observed geoid anomalies of slab origin (See Fig. 6(b)), that is, the geoid lows over the subduction zones. However, as γ decreases, the geoid anomalies reverse, that is, the geoid anomalies near the subduction zones become positive. This phenomenon has already been noted by Zhong and Davies (1999) for 3-D spherical geometry. By W model, the geoid high in the central Pacific and Africa is reproduced for all the γs. As γ decreases, the geoid anoma-
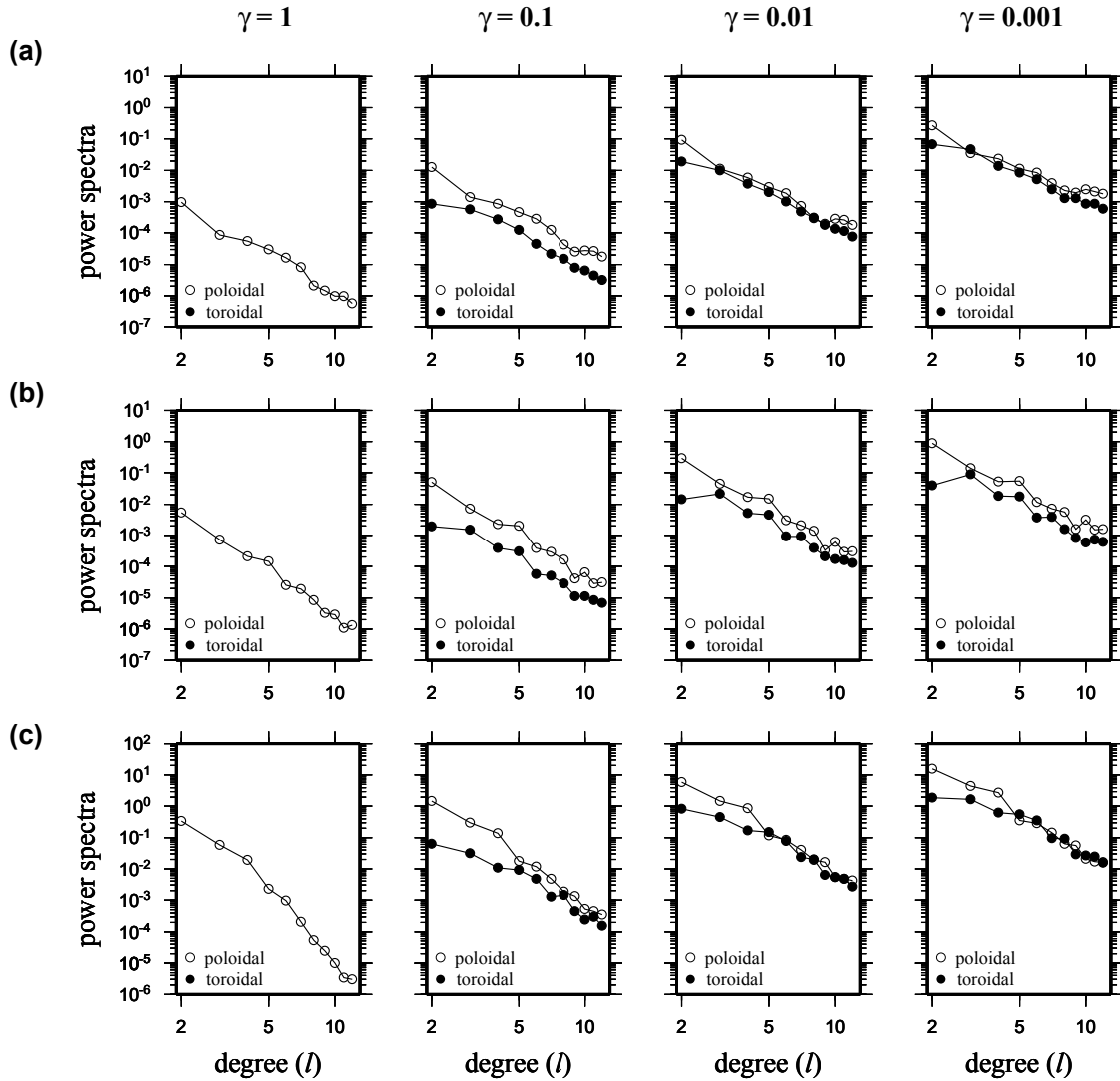
Fig. 4. Power spectra of the poloidal and toroidal velocity fields for U1 (a), U2 (b) and W (c).

lies related to the subduction, such as those of South Western Pacific and South America, become positive. This sign reversal of subduction related geoid anomalies appears to be reflected in the power spectra of the geoid anomalies versus the spherical harmonic degree *l* (Fig. 8). For the smallest γ (=0.001), the power spectra becomes flatter which implies the emergence of the high degree components. This is probably associated with the reversal of the geoid high related to the subducted slabs, as described before.

3.3   Intraplate stress

Figure 9 shows the orientations of the maximum principal horizontal stress axes (thick bars refer to the extension and thin bars refer to the compression) and gray scale for the stress magnitude (see below) calculated for all the density models. The stress magnitude is defined by the second invariant of the deviatoric stress,

$$\tau_{\mathrm{II}} = \sqrt{\frac{1}{2} \sum_{i,j=1}^{3} \tau_{ij} \tau_{ij}}, \qquad (15)$$

where τ_{ij} $(i, j = r, \theta, \phi)$ is the deviatoric stress tensor.

For all the models, regardless of the change of γ, the high

stress is observed at the edge of the plate and the subduction zones because of the increase of the strain rate there. For W model with $\gamma = 1$ (i.e., without weak margins), the stress magnitude near the subduction zones becomes of the order of 10 MPa. When γ decreases to 0.001, the stress near the subduction zones is of the order of 100 MPa (The stress magnitude at the weak margins is lower (of the order of 1 MPa) because of their low viscosity). Much area show an extensional feature, which is in contrast with the actual intraplate stress field characterized by a compressional stress (Richardson, 1992). This may imply that the other forces like those associated with the lithospheric thickening and the buoyancy of the crust may be necessary to explain the stress field.

4.   Conclusion and Discussions

We have conducted a preliminary numerical calculation of the instantaneous 3-D viscous flow in a spherical shell driven by the negative buoyancy forces due to subducted slabs in order to understand the influence of lateral variations in lithospheric viscosity, that is, the stiff plate interiors and the weak plate margins, on the present-day plate
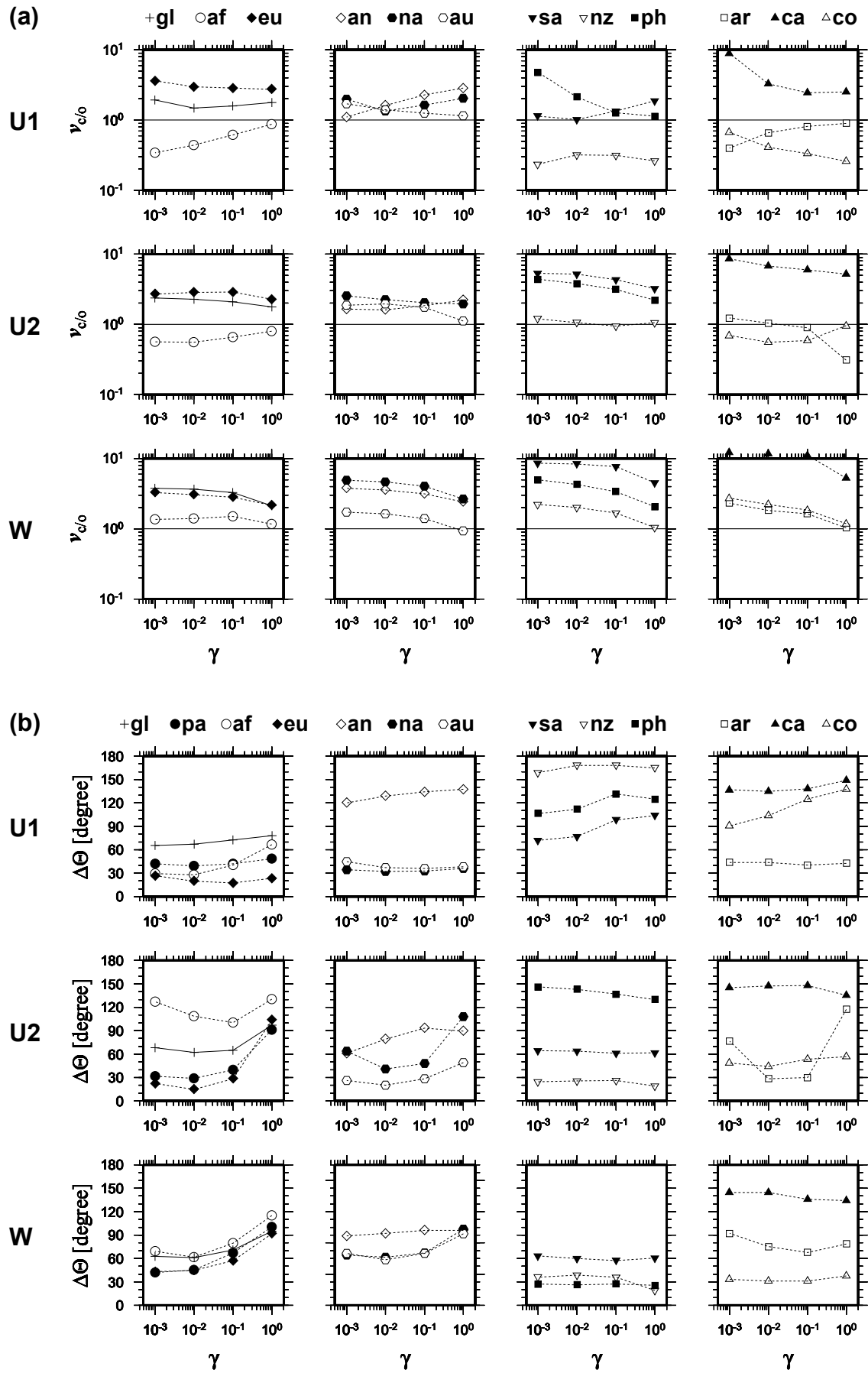
Fig. 5. (a) $v_{c/o}$ of 12 plates for U1, U2 and W. Abscissa is γ. Abbreviations of plate name in the figure are given in Fig. 1(b). (b) $\Delta\Theta$ of 12 plates for U1, U2 and W. Abscissa is γ. Abbreviations of plate name in the figure are given in Fig. 1(b).

Table 4. Results of $v_{c/o}$. $v_{c/o}$ of the Pacific plate is not included. See text for detail.

Plate	U1 $\gamma = 1$	U1 $\gamma = 0.001$		U2 $\gamma = 1$	U2 $\gamma = 0.001$		W $\gamma = 1$	W $\gamma = 0.001$		Model
af	0.871	0.341	−	0.804	0.566	−	1.17	1.37	(−)	W, U1, U2
eu	2.75	3.61	+	2.26	2.71	(−)	2.12	3.29	−	U2, (W, U1)
an	2.83	1.10	+	2.22	1.64	+	2.41	3.77	−	U1, U2, W
na	2.05	1.99	(+)	1.96	2.55	−	2.65	4.89	−	U1, U2, W
au	1.16	1.67	−	1.12	1.88	−	0.929	1.71	−	(U1, U2, W)
sa	1.86	1.14	+	3.23	5.34	−	4.52	8.53	−	U1, U2, W
nz	0.261	0.233	(−)	1.06	1.20	(−)	1.04	2.21	−	U2, W, U1
ph	1.13	4.76	−	2.21	4.36	−	2.05	4.96	−	(U2, U1, W)
ar	0.896	0.397	−	0.310	1.23	+	1.03	2.31	−	U2, W, U1
ca	2.51	8.81	−	5.19	8.59	−	5.27	12.3	−	(U2, U1), W
co	0.258	0.666	+	0.955	0.693	−	1.18	2.71	−	(U2, U1), W
All	1.77	1.92	(−)	1.78	2.39	−	2.12	3.78	−	U1, U2, W

Table 5. Results of $\Delta\Theta_{RMS}$. See text for detail.

Plate	U1 $\gamma = 1$	U1 $\gamma = 0.001$		U2 $\gamma = 1$	U2 $\gamma = 0.001$		W $\gamma = 1$	W $\gamma = 0.001$		Model
pa	48.4	42.2	(+)	91.2	31.7	+	100	41.9	+	U2, (U1, W)
af	66.8	29.6	+	131	127	(+)	115	69.3	+	U1, W, U2
eu	23.3	26.6	(−)	104	22.2	+	91.7	43.0	+	(U2, U1), W
an	137	120	(+)	89.6	61.1	+	96.2	88.7	(+)	U2, W, U1
na	36.2	34.4	(+)	108	63.7	+	97.6	64.2	+	U1, (U2, W)
au	38.3	44.5	(−)	48.9	26.2	+	91.5	66.4	+	U2, U1, W
sa	104	71.9	+	61.5	64.2	(−)	60.7	63.2	(−)	(W, U2), U1
nz	165	159	(+)	18.9	24.4	−	19.0	36.2	−	U2, W, U1
ph	125	106	(+)	130	146	(−)	25.4	27.2	(−)	W, U1, U2
ar	42.7	43.8	(−)	118	76.4	+	78.5	92.0	−	U1, U2, W
ca	149	137	(+)	135	145	(−)	134	144	(−)	U1, (W, U2)
co	138	90.8	+	56.7	48.5	(+)	37.6	33.5	(+)	W, U2, U1
All	78.1	65.3	(+)	96.8	68.3	+	95.1	62.5	+	(W, U1, U2)
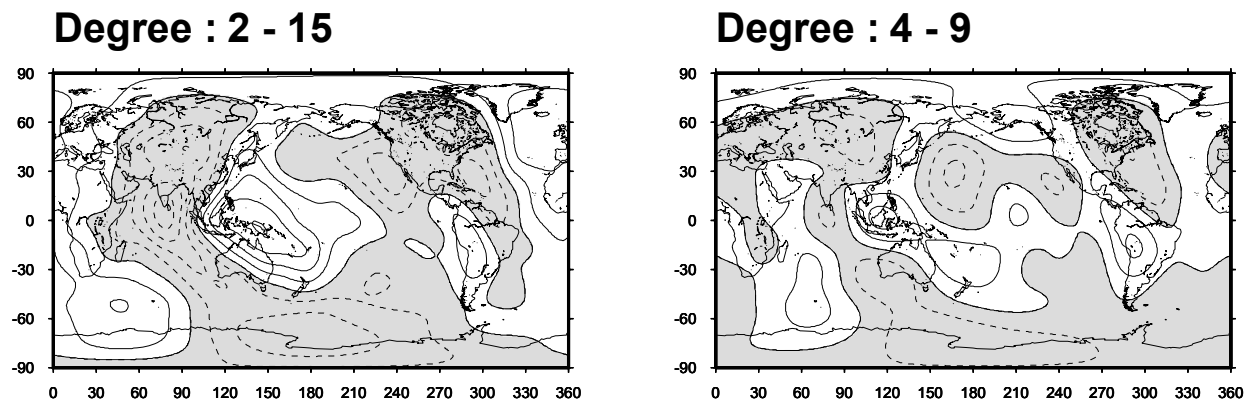
Fig. 6.   The observed geoid anomalies computed from the GEM-T3 Model (Lerch *et al.*, 1994) for $2 \leq l \leq 15$ (left) and $4 \leq l \leq 9$ (right). Contour interval is 20 m, and geoid lows are shaded. Continental shore lines are shown.

$\gamma = 1$ $\gamma = 0.01$ $\gamma = 0.001$

(a) contour intervals : 5 [m]

(b) contour intervals : 5 [m]

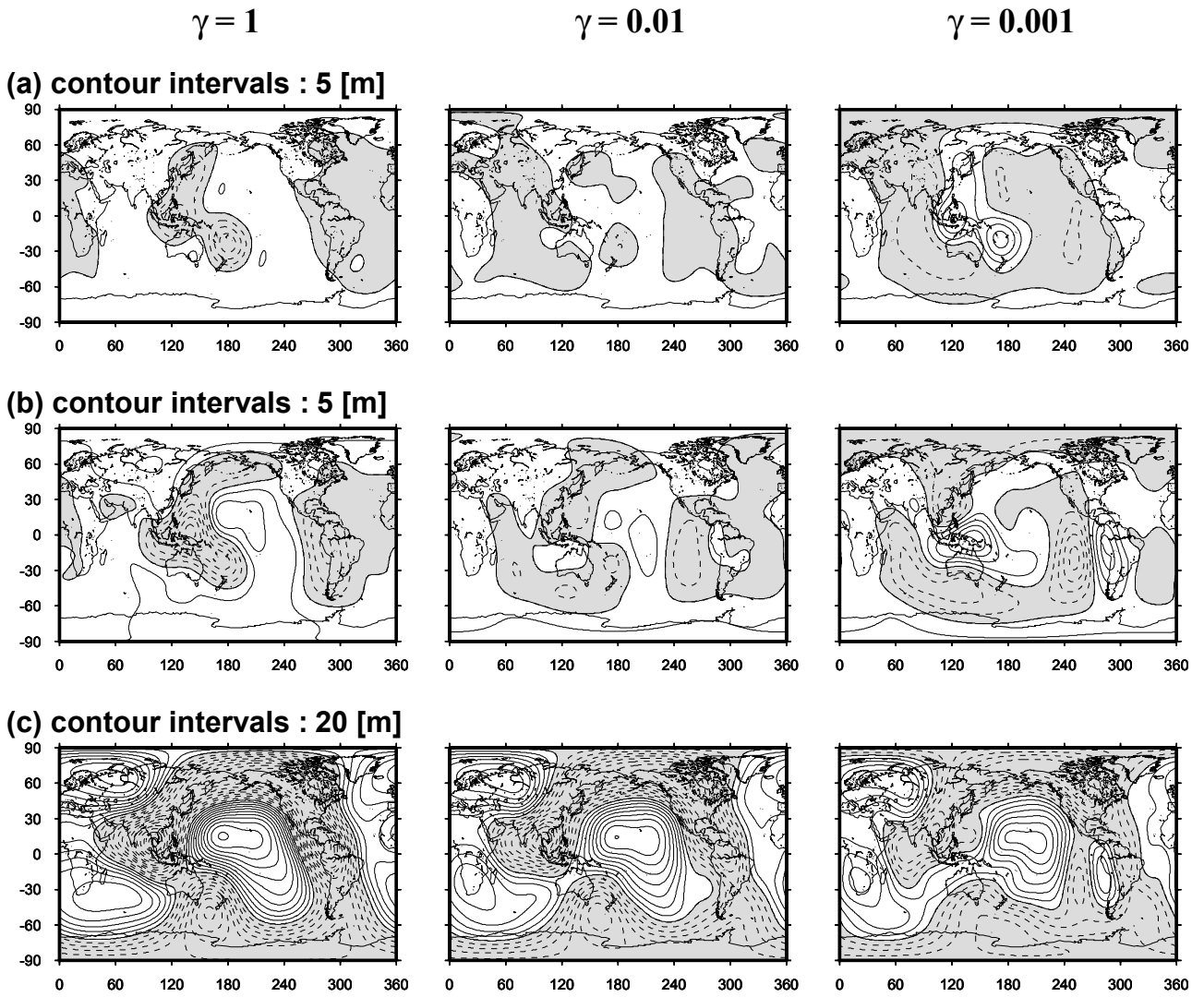**(c) contour intervals : 20 [m]**

Fig. 7. The geoid anomalies for U1 (a), U2 (b) and W (c). Contour interval is 5 m (a) and (b), 20 m (c), geoid lows are shaded. Continental shore lines are shown.
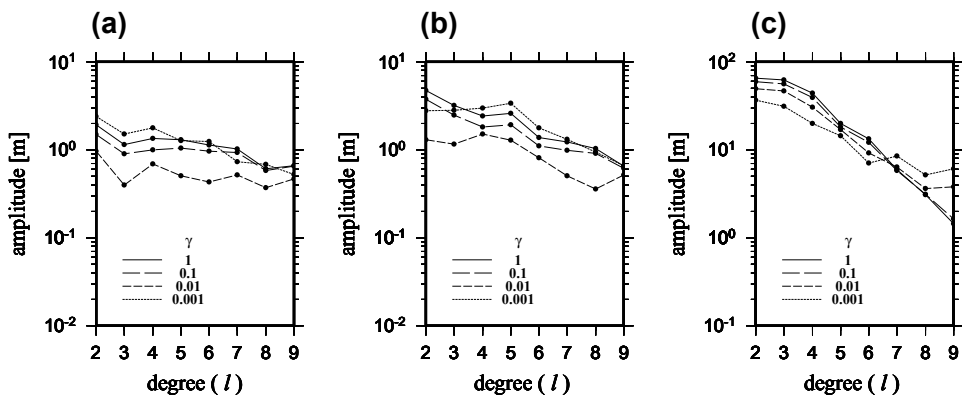
(a)   **(b)**   **(c)**

Fig. 8. Power spectra of calculated geoid anomalies for U1 (a), U2 (b) and W (c).

motions, geoid anomalies and the intraplate stresses. The density heterogeneity models used in this study are those inferred from seismicity associated with the subducting slabs and the history of subduction.

The ratio of the viscosity at the weak plate boundaries to that of the lithosphere (γ) are changed from 1 (i.e., without weak margin) to 0.001. We see an indication of plate-like behavior at $\gamma = 0.001$. The toroidal power of the ve-
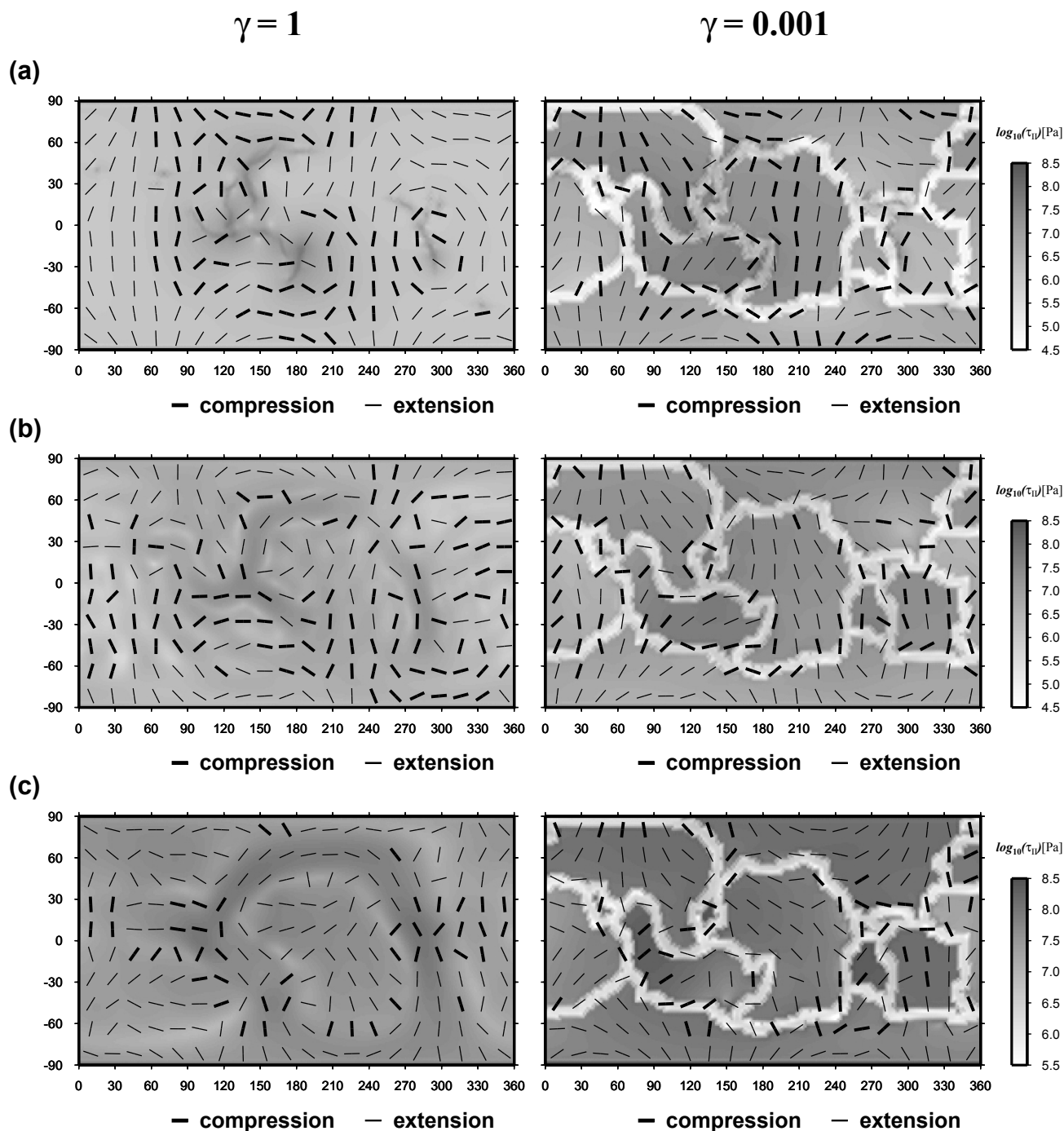
Fig. 9. Stress field for U1 (a), U2 (b) and W (c) with $\gamma = 1$ (right) and $\gamma = 0.001$ (left). Bars show the orientations of the maximum principal stress axes. The thick bars show the compression and the thin bars show the extension. Gray scale is used to show the logarithm of the magnitude of stress in the unit of Pa.

locity becomes comparable to the poloidal energy around $\gamma = 0.01$ and less. For W model, almost all the plates move too fast relative to the Pacific plate. This may imply (1) incomplete modeling of one-sided subduction, (2) overestimation of lower mantle load and/or (3) underestimation of lower mantle viscosity. It appears that the density models confined in the upper mantle are sufficient to explain the overall pattern of plate motions. The magnitude of the velocity can be adjusted by changing the reference viscosity and the difference of the direction of velocity may be ad-

justed by assuming the 'aseismic' density anomaly along the subduction zones.

For the whole mantle density model, the power spectra of the geoid anomalies become flatter as γ decreases. This may be caused by the change of the geoid anomalies related to the upper mantle slabs with the decrease of γ. Thus, our results generally support Zhong and Davies (1999)'s conclusion that the inclusion of the weak plate margins affects the long-wavelength components of the geoid anomalies. Our calculation does not include the effects of self-gravitation.

By analyzing the geoid kernels with and without self-gravitation obtained for the cases with no lateral variation of viscosity, we found that the amplitude of the geoid anomalies of $l = 2$ component becomes halved, while that of $l = 4$ or larger is not significant. Since our main interest is not to reproduce the observed geoid anomalies but to investigate the effects of weak plate margins on the geoid anomalies, we believe that our main conclusion is valid. However, it is necessary to include the self-gravitation in the future modeling aiming at the reproduction of observed geoid anomalies.

The intraplate stress shows a prevalence of an extension. This is in contrast with the actual intraplate stress field characterized by a general compression. Various types of the forces are proposed for the driving mechanism of plate motions (Forsyth and Uyeda, 1975). Forsyth and Uyeda (1975) concluded that the main source of the stress in the lithosphere is a negative buoyancy force due to the descending plates which are included in our density heterogeneity models. The other important mechanism is the lithosphere thickening caused by the cooling of the lithosphere as it moves away from ocean ridges (Hager, 1978; Turcotte and Schubert, 1982). Richardson (1992) suggests that the ridge push force may account for the broad feature of the global intraplate stress field. Such a factor should be included in the future.

The horizontal resolution of our numerical models, which is a few hundred kilometers, in this study is probably poor. The width of the realistic plate margins, which might be of the order of fault width, is supposed to be very narrow (Zhong and Gurnis, 1996; Zhong *et al.*, 1998). Such a feature might not be able to be approximated by the broad low viscosity zones at the plate boundaries.

References

Argus, D. F. and R. G. Gordon, No-net-rotation model of current plate velocities incorporating plate motion model NUVEL-1, *Geophys. Res. Lett.*, **18**, 2039–2042, 1991.

Bai, W., C. Vigny, Y. Ricard, and C. Froidevaux, On the origin of deviatoric stresses in the lithosphere, *J. Geophys. Res.*, **97**, 11729–11737, 1992.

Christensen, U. and H. Harder, 3-D convection with variable viscosity, *Geophys. J. Int.*, **104**, 213–226, 1991.

Corrieu, V., C. Thoraval, and Y. Ricard, Mantle dynamics and geoid Green functions, *Geophys. J. Int.*, **120**, 516–523, 1995.

Forsyth, D. W. and S. Uyeda, On the relative importance of the driving force of plate motion, *Geophys. J. R. Astron. Soc.*, **43**, 163–200, 1975.

Gordon, R. J. and D. M. Jurdy, Cenozoic global plate motions, *J. Geophys. Res.*, **91**, 12389–12406, 1986.

Gurnis, M., J. X. Mitrovica, J. Ritsema, and H.-J. van Heijst, Constraining mantle density structure using geological evidence of surface uplift rates: The case of the African superplume, *Geochemist. Geophys. Geosyst.*, **1**, 1999GC000035, 2000.

Hager, B. H., Oceanic plate motions driven by lithospheric thickening and subducted slabs, *Nature*, **276**, 541–545, 1978.

Hager, B. H., Subducted slabs and the geoid: Constraints on mantle rheology and flow, *J. Geophys. Res.*, **89**, 6003–6015, 1984.

Hager, B. H. and R. W. Clayton, Constraints on the structure of mantle convection using seismic observations, flow models and the geoid, in *Mantle Convection: Plate Tectonics and Global Dynamics*, edited by W. R. Peltier, The fluid mechanics of astrophysics and geophysics 4, pp. 657–763, Gordon and Breach Science Publishers, New York, 1989.

Hager, B. H. and R. J. O'Connell, Subduction zone dip angles and flow driven by plate motion, *Tectonophys.*, **50**, 111–133, 1978.

Hager, B. H. and R. J. O'Connell, A simple global model of plate dynamics and mantle convection, *J. Geophys. Res.*, **86**, 4843–4867, 1981.

Hager, B. H., R. W. Clayton, M. A. Richards, R. P. Comer, and A. M. Dziewonski, Lower mantle heterogeneity, dynamic topography and the geoid, *Nature*, **313**, 541–545, 1985.

Iwase, Y., Three-dimensional infinite Prandtl number convection in a spherical shell with temperature-dependent viscosity, *J. Geomag. Geoelector.*, **48**, 1499–1514, 1996.

Karato, S.-I. and P. Wu, Rheology of the upper mantle: A synthesis, *Science*, **260**, 771–778, 1993.

Lerch, F. J. and 19 others, A geopotential model from satellite tracking, altimeter and surface gravity data: GEM-T3, *J. Geophys. Res.*, **99**, 2815–2839, 1994.

Moresi, L. and M. Gurnis, Constraints on the lateral strength of slabs from three-dimensional dynamic flow models, *Earth Planet. Sci. Lett.*, **138**, 15–28, 1996.

Ricard, Y. and C. Vigny, Mantle dynamics with induced plate tectonics, *J. Geophys. Res.*, **94**, 17543–17559, 1989.

Ricard, Y., M. A. Richards, C. Lithgow-Bertelloni, and Y. L. Stunff, A geodynamics model of mantle density heterogeneity, *J. Geophys. Res.*, **98**, 21895–21909, 1993.

Richards, M. A. and B. H. Hager, Effects of lateral viscosity variations on long-wavelength geoid anomalies and topography, *J. Geophys. Res.*, **94**, 10299–10313, 1989.

Richardson, R. M., Ridge forces, absolute plate motions, and the intraplate stress field, *J. Geophys. Res.*, **97**, 11739–11748, 1992.

Tackley, P. J., Three-dimensional simulations of mantle convection with a thermo-chemical basal boundary layer: D"?, in *The Core-Mantle Boundary Region*, edited by M. Gurnis, M. E. Wysession, E. Knittle, and B. A. Buffett, Geodynamics series 28, pp. 231–253, American Geophysical Union, Washington, D.C., 1998.

Turcotte, D. L. and G. Schubert, *Geodynamics: Applications of Continuum Physics to Geological Problems*, pp. 450, John Wiley and Sons, New York, 1982.

Wen, L. and D. L. Anderson, Present-day plate motion constraint on mantle rheology and convection, *J. Geophys. Res.*, **102**, 24639–24653, 1997.

Zhang, S. and U. Christensen, Some effects of lateral viscosity variations on geoid and surface velocities induced by density anomalies in the mantle, *Geophys. J. Int.*, **114**, 531–547, 1993.

Zhong, S. and G. F. Davies, Effects of plate and slab viscosities on the geoid, *Earth Planet. Sci. Lett.*, **170**, 487–496, 1999.

Zhong, S. and M. Gurnis, Interaction of weak faults and non-Newtonian rheology produces plate tectonics in a 3D model of mantle flow, *Nature*, **383**, 245–247, 1996.

Zhong, S., M. Gurnis, and L. Moresi, Role of faults, nonlinear rheology, and viscosity structure in generating plates from instantaneous mantle flow models, *J. Geophys. Res.*, **103**, 15255–15268, 1998.

Zoback, M. L., First- and second-order patterns of stress in the lithosphere: The world stress map project, *J. Geophys. Res.*, **97**, 11703–11728, 1992.

Zoback, M. L. and 27 others, Global patterns of tectonic stress, *Nature*, **341**, 291–298, 1989.

M. Yoshida (e-mail: myoshida@eri.u-tokyo.ac.jp), S. Honda, M. Kido, and Y. Iwase